

Shock ignition target design for inertial fusion energy

Andrew J. Schmitt,^{1, a)} Jason W. Bates,¹ Steven P. Obenshain,¹ Steven T. Zalesak,² and David E. Fyfe³

¹⁾Plasma Physics Division, Naval Research Laboratory, Washington DC 20375

²⁾Berkeley Research Associates, Beltsville MD 20705

³⁾LCP&FD, Naval Research Laboratory, Washington DC 20375

(Dated: 1 December 2009; Accepted for Publication: 18 March 2010)

Continuing work in the design of shock ignition targets is described. Because of reduced implosion velocity requirements, low target adiabats, and efficient drive by short wavelength lasers, these targets produce high gain (> 100) at laser energies well below 1 megajoule. Effects of hydrodynamic instabilities like Rayleigh-Taylor or Richtmyer-Meshkov are greatly reduced in these low-aspect ratio targets. Of particular interest is the optimum ratio of ignitor to compression pulse energy. A simple pellet model and simulation-derived coupling coefficients are used to analyze optimal fuel assembly, and determine that shock ignition allows enough control to create theoretically optimum assemblies. The effects on target design due to constraints on the compression and ignitor pulse intensities are also considered and addressed. Significant sensitivity is observed from low-mode perturbations because of large convergence ratios, but a more powerful ignitor can mitigate this.

I. INTRODUCTION

Shock ignition is a new concept for producing inertial confinement fusion (ICF), although it has precursors in earlier research¹. Like conventional central ignition ICF, it relies on a small central hot spot that ignites and burns the surrounding cold high density fuel. However, in shock ignition the target compression and ignition are produced by two distinct parts of the laser pulse: a compression pulse and a short, high intensity ignitor pulse respectively.

Analysis indicates that shock ignition can produce much higher gains at low laser energies than conventional ignition^{2,3}. Simulations find that significant gains could be achieved with as little as ~ 250 kJ of $0.248\mu\text{m}$ wavelength light. One-dimensional (1D) gains of 100 are possible for laser energies of about a quarter-megajoule, and gains are comparable to fast ignition schemes⁴. In high resolution two-dimensional (2D) simulations that include single nonuniformity sources, targets provide nearly full 1D gains with expected levels of outer perturbations, inner perturbations, or ISI imprint. The short wavelength and zooming capabilities of the Krypton Fluoride (KrF) laser result in much more efficient drive, and higher gains, than frequency-tripled glass lasers.

This paper summarizes results from new shock ignition design studies. We are particularly interested here in the optimal separation of the laser pulse energy into the target compression and hot-spot ignition. Like fast ignition, shock ignition promises independent control of heating and compression of the hot spot and cold fuel. We benchmark a simple theoretical model that predicts an optimal splitting of the pellet energy, and investigate the coupling between the compression and ignitor pulses and the pellet assembly components. Such control implies that there is a continuum of designs between shock ignition and conventional central ignition: with sufficiently high compression power the needed ignitor shock vanishes and one recovers conventional central ignition. This offers much flex-

ibility in the design of high performance implosions.

Because of the reduced implosion velocity requirements in shock ignition, one can use compression intensities that are smaller than needed for conventional ignition; alternatively, the target radius and aspect ratio (AR) can be reduced to produce more stability. The latter approach is taken here, so intensities are limited by the need to avoid laser-plasma instabilities (LPI) during compression. The actual limits, however, are uncertain. Previous studies at $0.35\mu\text{m}$ laser wavelength have suggested that the two plasmon decay instability begins to be of concern in the neighborhood of $\sim 5 - 8 \times 10^{14} \text{ W/cm}^{25-7}$. When the intensity increases past this limit, the instabilities show nonlinear behavior and are not well described by existing theory. Results from recent LPI experiments on the Nike KrF laser ($0.248\mu\text{m}$ wavelength) are consistent with an intensity limit of about a factor of two higher^{8,9}, and further experiments are planned. Whatever the limits, the compression intensity determines the pressure that drives the pellet, and ultimately the hydrodynamic instability growth and yield that can be achieved.

In contrast, the high shock pressures needed for ignition require ignitor intensities higher than these limits, and LPI will likely be active. When the ignitor is applied, however, the target has an areal density large enough to shield itself from hot electrons below about $\sim 100\text{keV}^{10}$. Indeed, the production of hot electrons during the ignitor may actually raise the ignitor coupling efficiency¹¹. Thus the ignitor may be constrained as much by the laser capability as by fundamental interaction physics issues. In this paper, we do not simulate LPI effects but instead examine the tradeoffs that may be possible to avoid possible intensity constraints.

The results presented here are separated into two parts; the first section deals with design work in 1D using the FAST radiation hydrocode¹², and examines limits and tradeoff in parameters determining the compression and ignitor pulse intensities. Simulation results are compared to a simple model of the assembled pellet, and the limits of constructing optimal configurations are examined. Options for changing the intensities of the laser pulses are also examined. The second section reports on 2D FAST simulation results, and considers the effects of hydrodynamic instabilities and limits of target

^{a)}Electronic mail: andrew.schmitt@nrl.navy.mil

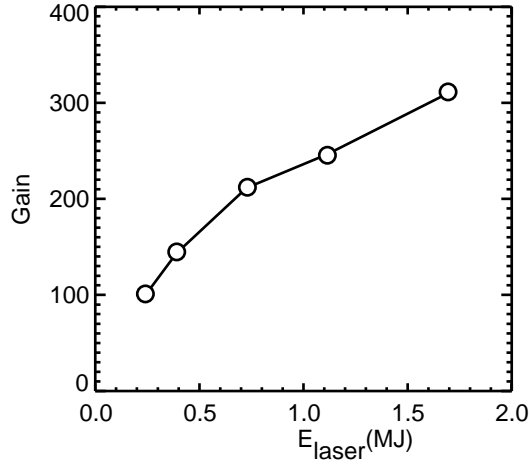


FIG. 1. The 1D gain curve constructed from the optimum gain cases at each scale factor for the shock ignition targets simulated in this study.

perturbations. Options for coping with the high convergence ratios and intensity limitations are presented and discussed.

II. 1D STUDIES

The shock ignition targets examined here are DT-ice fuel shells within low-density wetted-and-frozen DT foam ablaters, and have a low initial aspect ratio ($R/\Delta R = 2.5$). The target mass is varied by a factor of 16, with the aspect ratio and initial shock pressure remaining the same (see Table I). A relaxation pulse¹³ drives the target. An initial picket containing less than a percent of the total laser energy induces a ~ 50 Mbar decaying shock through the target. This is followed by a foot pulse with a shock pressure of ~ 3 Mbar, driven by an intensity of ~ 6 TW/cm². Further shock-free compression leads to a $1/e$ mass-averaged adiabat between 1.8-2. (The adiabat is defined as the ratio of the pressure to the Fermi-degenerate pressure). This shock-free compression is done by the remaining compression pulse, which rises to peak powers producing pressures of 100's of Mbar. Finally, a short pulse, high intensity “spike” is applied just before stagnation, producing a shock of order 1 Gbar. The ignitor start is contiguous with the end of the compression pulse. Laser-pellet coupling is optimized by zooming the laser (i.e., shrinking the focal spot) twice during the implosion¹⁴.

We optimize the target by varying the compression power and the ignitor⁴. The target is first tuned by selecting a compression power (without an ignitor) and maximizing the peak areal density. Then, a variety of ignitor pulses, defined by their peak power, pulse width, and turn-on time (“timing”) are applied and gain is optimized. The compression power is changed and the process is repeated. This maps out a region in a four-parameter space that produces the highest gains. Selecting the best gain achieved at each pellet scale produces the gain curve (Fig. 1).

TABLE I. Target specifications, listed by relative mass. In all cases, the ablator is made of 100mg/cm³ CH foam wicked with solid DT, the fuel layer is DT ice. The target linear dimensions are scaled by the cube root of the scale factor, which denotes the relative target mass. Simulation parameters listed are those found at highest gain.

Scale (relative mass)	1×	2×	5×	8×	16×
Outer Radius (μm)	854	1076	1455	1708	2152
Ablator Thickness (μm)	108	136	177	216	272
Fuel Thickness (μm)	237	300	407	476	600
Best gain	101	143	210	243	309
E_{laser} (kJ)	231	390	727	1074	1700
Absorption (%)	80	85	87	91	93
IFAR	21	20	16	14	11
ρR (g/cm ³)	2.4	2.9	3.4	3.4	4.0
Ignitor power (TW)	300	400	450	500	750
Ignitor pulse width (ps)	200	250	500	400	550
Compression power (TW)	95	110	120	160	150
In-flight adiabat	2.0	2.0	1.9	1.7	1.8
$V_{\text{implosion}}$ ($\times 10^7$ cm/s)	2.8	2.6	2.2	2.2	1.9
$E_{\text{ignitor}}/E_{\text{laser}}$	0.18	0.19	0.21	0.13	0.20
$C_r [R_0/R_{\text{hot spot min}}]$	63	65	68	52	65

A. Optimization of Compression Power

A priori, it is unknown what compression power produces the best gain. The implosion velocity should be smaller than needed for ignition, yet high enough to give significant compression. As a rule of thumb, we begin using compression powers that produce implosion velocities of $\sim 2 - 2.5 \times 10^7$ cm/sec (for the scale-2 target, the minimum ignition velocity, without an ignitor, is $\gtrsim 3 \times 10^7$ cm/sec).

The best gain typically occurs at compression powers less than 50% of that needed for conventional ignition (Fig. 2), but the optimized gains are relatively insensitive to changes in the compression power. As the power increases, the compression pulse alone becomes large enough to ignite the pellet, and the ignitor is no longer needed. The gain drops towards this limit as the laser energy requirements become larger. (This ignitor-less limit would be precluded in practice because the intensities needed to achieve it [Fig. 2b] are well above LPI limitations.) Thus, there is a continuum between shock ignition and conventional central ignition. For smaller compression powers, the ignitor energy grows and the timing tolerance narrows. As the ignitor increases, the coronal plasma becomes hotter, the absorption drops and the shock launch time moves closer to the stagnation time. Simultaneously, the lower compression power produces smaller ρR and lower gains follow.

Predictions of optimum compression power require knowledge of (a) the optimum configuration of the imploded and assembled fuel and (b) the coupling between the laser pulse components and the assembled pellet components. We consider coupling in section II B; here we turn our attention to the optimum fuel assembly. A simple Meyer-ter-Vehn-type analysis¹⁵ can be used to show that for optimally assembled targets, the hot spot energy should be much smaller than the

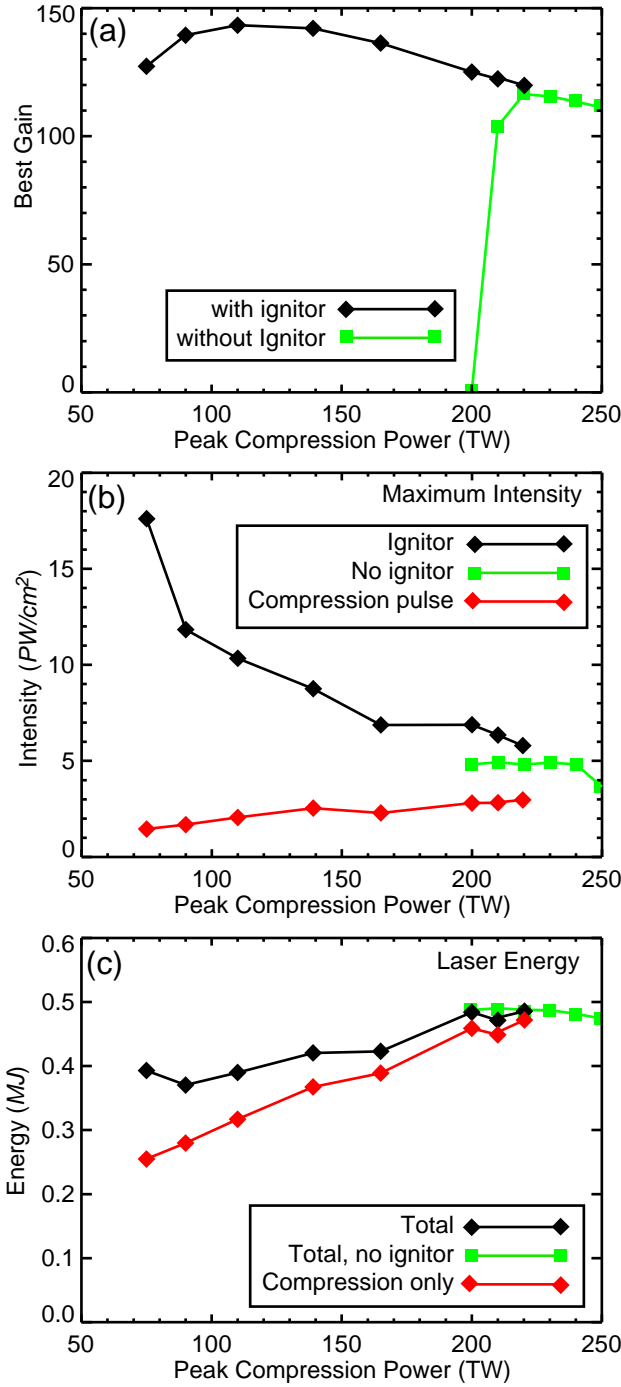


FIG. 2. (Color online) (a) Optimum gain, (b) peak laser intensities, and (c) laser pulse energies as a function of compression power, for a 250 ps FWHM ignitor and the scale-2 target.

compression energy (see Appendix A), about 27 times smaller for an isobaric target. This hot-spot to cold-fuel energy ratio is larger for shock ignition targets, depending upon the pressure ratio between the hot spot and the cold fuel.

This model was verified with simulations of different scale targets and compression powers, using drive parameters that are optimal for the corresponding scale size and compression

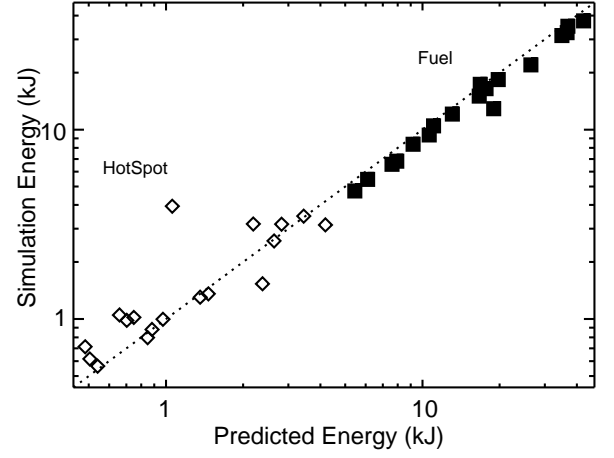


FIG. 3. Comparison of simulation and predicted hot-spot (open diamonds) and cold-fuel (solid squares) energies. The predicted energies use the formula from Table II in Appendix A, and the assembled fuel masses, stagnation adiabats, and hot-to-cold pressure ratios measured in the simulations.

power. To separate the effects of the pulse heating from alpha particle heating, thermonuclear burn is turned off. The pellet is considered fully assembled when the internal energy of the hot spot peaks. (The hot spot is defined as the fuel around $r = 0$ with a temperature of at least 1 keV, while the cold fuel is defined as the mass within $1/e$ of the peak density). Fig. 3 shows that the hot spot and cold fuel energies from the simulation scale according to the predictions from this model.

The laser compression and ignitor pulses separately affect the components of an optimal configuration. In the next section we examine the contributions of each part of the laser pulse (compression vs. ignitor) to the two assembled fuel regions.

B. Coupling

In conventional ignition, the laser pulse couples a fraction of its energy to the pellet, known as the coupling efficiency. However, knowledge of this single fraction is insufficient to optimize the pellet, since we wish to independently control the pellet's hot spot and cold fuel with the compression and ignitor pulses. Both of these two pulses produce pellet compression and heating, but in different ways. The compression pulse compresses and accelerates the fuel shell, producing kinetic energy which is then converted into internal energy when the pellet stagnates. The ignitor delivers energy through the spherically convergent shock it producing shock heating and $p - dV$ work. Because of their very different intensities, the absorption is also markedly different for the two pulses. We wish to know if the coupling of these two pulses to the hot spot and fuel is different enough to produce a truly optimal pellet configuration.

We first construct the coupled equations that relate hot-spot and cold-fuel energy to the compression and ignitor pulse en-

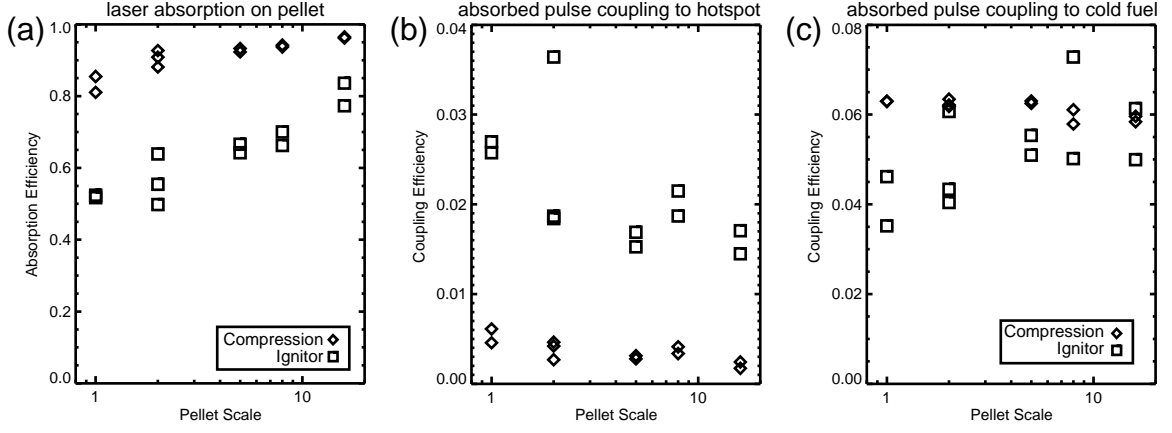


FIG. 4. Absorption and coupling efficiencies for the laser pulse to the pellet ignition assembly. The coupling efficiencies have the absorption factored out, i.e., they denote coupling of absorbed energies. The diamond symbols denote the laser compression pulse, and the square symbols denote ignitor pulse coupling.

ergies:

$$\bar{e}_{\text{pellet}} = \bar{\bar{M}} \bar{e}_{\text{laser}} \quad (1)$$

where $\bar{e}_{\text{pellet}} = [e_{\text{hotspot}}, e_{\text{coldfuel}}]$, $\bar{e}_{\text{laser}} = [e_{\text{ignitor}}, e_{\text{compression}}]$ and

$$\bar{\bar{M}} = \begin{vmatrix} \epsilon_{hi} & \epsilon_{hc} \\ \epsilon_{ci} & \epsilon_{cc} \end{vmatrix} \quad (2)$$

is the coupling matrix. If the matrix is diagonally dominant, then we have independent control of the energy in the pellet hot spot and the cold fuel.

Next the laser pulse energies are found as $\bar{e}_{\text{laser}} = \bar{\bar{M}}^{-1} \bar{e}_{\text{pellet}}$, or :

$$e_{\text{ignitor}} = (\epsilon_{cc} e_{\text{hotspot}} - \epsilon_{hc} e_{\text{coldfuel}}) / \det(M) \quad (3)$$

$$e_{\text{compression}} = (-\epsilon_{ci} e_{\text{hotspot}} + \epsilon_{hi} e_{\text{coldfuel}}) / \det(M) \quad (4)$$

where $\det(M) = \epsilon_{hi} \epsilon_{cc} - \epsilon_{hc} \epsilon_{ci}$. Thus the ratio of the ignitor energy to the laser compression energy is:

$$\frac{e_{\text{ignitor}}}{e_{\text{compression}}} = \frac{\epsilon_{cc} \frac{e_{hs}}{e_{cf}} - \epsilon_{hc}}{\epsilon_{hi} - \epsilon_{ci} \frac{e_{hs}}{e_{cf}}} \quad (5)$$

Assuming all the coupling coefficients are positive, this relation is only positive in the range:

$$\epsilon_{hc} / \epsilon_{cc} \leq e_{hs} / e_{cf} \leq \epsilon_{hi} / \epsilon_{ci}, \text{ or} \quad (6)$$

$$\epsilon_{hi} / \epsilon_{ci} \leq e_{hs} / e_{cf} \leq \epsilon_{hc} / \epsilon_{cc}. \quad (7)$$

For a diagonally dominant coupling matrix, only the first condition applies. This inequality shows that there is a limited range of hot-spot to cold-fuel energies in the pellet assemblies that can be formed.

We find the coupling values with a set of simulations at each pellet scale. Compression powers are sampled at optimal, low, and high values. To separate pulse heating effects

from nascent thermonuclear burn, burn is turned off. Simulations with and without ignitors determine its additional heating. Typical values (see Fig. 4) for the coupling efficiencies show that the coupling matrix is diagonally dominant: $\epsilon_{hi} \sim 1 - 1.5\%$ and $\epsilon_{hc} \sim 0.2 - 0.5\%$, while $\epsilon_{cc} \sim 5 - 6\%$ and $\epsilon_{ci} \sim 2 - 4.5\%$. Although the coupling is not completely orthogonal, the ignitor preferentially couples its energy to the hot spot while the compression pulse couples more to the cold fuel.

The limits of the ratio e_{hs}/e_{cf} that can be produced by shock ignition can be approximated by using the following average values for the net coupling coefficients: $\epsilon_{hi} = 0.01$, $\epsilon_{hc} = 0.003$, $\epsilon_{cc} = 0.055$ and $\epsilon_{ci} = 0.025$. This predicts that we can create pellets with $0.055 \leq e_{hs}/e_{cf} \leq 0.4$. According to the simple model in appendix A, the optimum ratio of e_{hs}/e_{cf} should be $\approx \Phi/27$. In the targets simulated here $\Phi \approx 2 - 3$ (without burn), so we expect optimal assemblies to have $e_{hs}/e_{cf} \approx 0.09 - 0.13$. If the coupling coefficients are assumed to be roughly constant, we would conclude that the optimum ignitor/compression energy ratio would be between 0.13 and 0.43. The observed ratios of ~ 0.25 (Table I) are in this range.

C. Laser Intensity

There is an upper limit on drive intensity which, if exceeded, can produce destructive laser-plasma interactions (LPI). This limit will be determined by the plasma conditions (primarily, temperature and density scalelength) and laser wavelength. Although the exact limit is currently unknown, current measurements suggest that it is less than 10^{15} W/cm^2 for $0.35 \mu\text{m}$ wavelength light⁵⁻⁷, and a factor of about two higher ($1.5 - 1.7 \times 10^{15} \text{ W/cm}^2$) for $0.248 \mu\text{m}$ wavelength light⁹. The primary LPI concern in direct-drive is the two-plasmon decay instability (TPD), because the threshold is low and it can generate electrons hot enough to penetrate and pre-heat the fuel. Stimulated Raman scattering (SRS), stimulated

Brillouin scattering (SBS) and the parametric decay instability (PD) are possible as well.

The intensity limit is most important during compression, since the pellet is most sensitive to preheat during this time. The compression intensity can be decreased by adjusting the pellet mass and/or aspect ratio, and also by changing the timing and zooming ratios. The drawback to these adjustments is their negative impact on hydro stability.

However, the ignitor pulse intensity *must* climb to $\sim 10^{16} \text{ W/cm}^2$ to produce an adequately strong igniting shock. This is clearly above projected LPI thresholds. As has been pointed out previously^{10,11}, the ignitor begins when the pellet areal mass has significantly increased due to convergence. The areal mass then ($\sim 0.05 - 0.06 \text{ gm/cm}^2$) can shield the pellet interior from electron temperatures of $\sim 100 \text{ keV}$ ¹⁰. LPI electrons lower than this limit may actually help to transport the laser energy deeper into the pellet ablator and enhance the igniting shock. However, if other LPI effects are destructive (e.g., reflecting too much light from absorption regions, or producing extremely hot electrons), it may be necessary to limit the laser intensity.

We examine the flexibility of controlling the intensity in these different parts of the pulse in the next two sections.

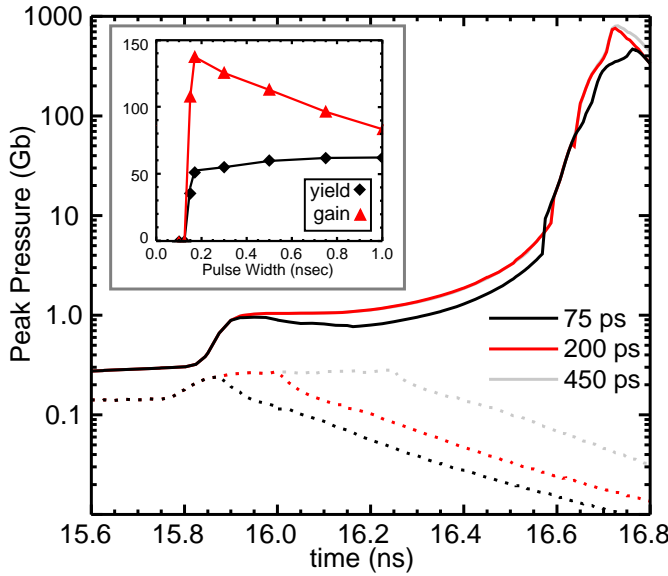


FIG. 5. (Color online) The ignitor shock pressures as a function of time, as the ignitor pulse width changes. The ignitor peak power is 450 TW. The solid lines are the peak shock pressures, while the dotted lines are the pressure at the laser critical surface. Inset: The pellet yield (black diamond) and gain (red triangle) vary with the ignitor pulse width.

1. Ignitor pulse flexibility

The ignitor pulse uses high intensities in order to produce the igniting shock. It can produce LPI but also heats the plasma corona, which decreases collisional absorption. There may also be driver limitations on either the ignitor pulse length

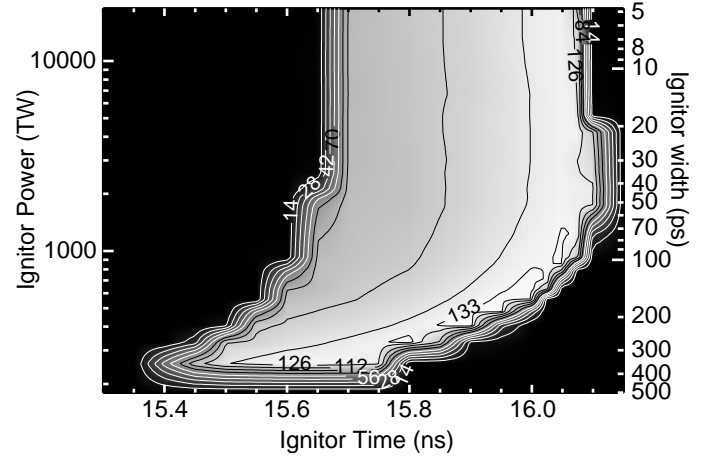


FIG. 6. The gain vs. ignitor timing and power (and pulse length), holding the ignitor energy fixed at 90 kJ.

or power¹⁶. Longer, lower power ignitors may be easier to generate, but short higher power ignitors may couple better. Here we examine the flexibility offered by trading off pulse power for pulse length at constant ignitor energy.

After the ignitor pulse launches its shock, it turns off and a rarefaction wave follows the shock. Geometric convergence increases the shock strength and accelerates it as it nears the target center. The rarefaction wave chases the shock and can overtake it and reduce its strength. For short pulse lengths the ignitor shock will not have time to reach full strength, and/or the rarefaction wave will catch and erode it. Increasing pulse lengths, after attaining ignition, can increase the pellet areal mass and increase burnup, but expend more energy and can reduce the gain. Thus, there may be some optimum pulse width.

First, we varied the ignitor pulse width at constant power (Fig. 5) in an optimally timed scale-2 target. The ignitor pulse rises linearly for 100 psec, and is then shut off at varying times. While the pressure at the critical surface responds immediately to the laser pulse turn-off, the peak shock pressure is unaffected once the pulse width exceeds 120 psec. By delaying the effects of the incoming rarefaction wave, larger pulse widths produce more fuel compression and areal mass, which increases the yield. However, the higher yield is more than offset by the increase in laser energy used in extending the ignitor. At constant power, the optimum width is just a little larger than the minimum needed to induce ignition. Although it is not evident here, a larger pulse width can be helpful in increasing the pellet robustness to 2D perturbations.

There is also a broad flexibility in trading off the ignitor power with its pulse width, at constant energy. Using the same target, we fix the energy at 90 kJ (approximately 20% of the compression energy, and typically the amount producing the optimum gain). The results (Fig. 6) show that the pulse length can be varied from 450 ns to less than $\sim 4 \text{ ps}$ while still keeping effectively the same gain; for most of these powers, the ignitor timing has a 350 psec range. At the high power/short pulse width end of this parameter range, the physics as simu-

lated here appears to be sensitive only to the deposited energy. In reality, such high powers would increasingly be affected by LPI, which is beyond the scope of this modelling.

2. Compression intensity

Because the incoming velocity requirements for shock ignition are significantly lower than those in conventional ignition, there is possibility of using lower compression intensity. On the other hand, for a given implosion velocity, a higher compression intensity will allow one to use more mass in the target (producing higher pellet yields) and/or to use lower aspect ratio targets (producing more hydrodynamic stability). Thus, there is still a strong incentive to use the highest intensity possible. In the targets presented so far, we have used compression intensities of about $2 \times 10^{15} \text{ W/cm}^2$. Here we investigate the tradeoffs involved in lowering this intensity with the scale-2 target.

The target was rescaled using the relations $R \sim I^{-1/3}$ and $\rho \Delta R \sim I^{0.45}$,¹⁷ which assume constant energy and velocity. After tuning the new targets, the ignitor is optimized for gain.

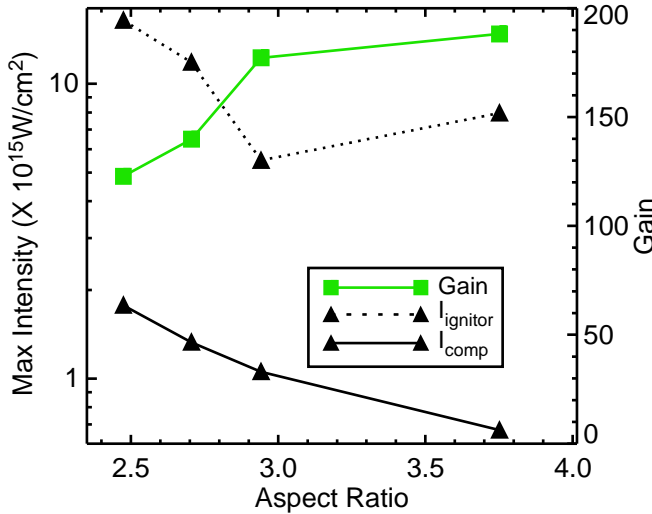


FIG. 7. (Color online) The maximum laser intensities and gains for scale-2 pellets rescaled to different initial aspect ratios. All targets have the same laser energy and implosion velocity (without ignitor).

The lowered intensity leads to a larger radius target with a larger initial aspect ratio: to achieve the same implosion velocity (about $2.4 \times 10^7 \text{ cm/sec}$), the pellet shell must be pushed further with the decreased pressure. Although the shell is thinner, it will have more mass ($m \sim R^2 \Delta R \sim I^{-0.22}$). Lower intensity also results in cooler temperatures and smaller ablation velocities, which give higher absorption and hydrodynamic efficiency. All of this leads to higher 1D yield and gain (Fig. 7). The drawback is that the pellet shell becomes more susceptible to hydrodynamic instabilities: it has more instability growth as the shell is driven longer distances, and the smaller mass ablation rate leads to less stabilization for high frequency perturbations. We shall return to this point in the

2D analysis.

III. 2D STUDIES

Two dimensional simulations are needed to assess the effect of nonuniformity sources and stability of the targets. The nonuniformities include pellet manufacturing imperfections (“surface perturbations”) as well as driver sources such as laser imprint or beam misalignment. These perturbations serve as seeds for hydrodynamic instabilities like Rayleigh-Taylor and Richtmyer-Meshkov.

Both low and high resolution two dimensional simulations are useful here. Low resolution simulations (typically 850 radial zones and 64 zones in inclination between $\theta = 0 - \pi$) are used to simulate low-mode nonuniformities; the range $\ell = 1 - 16$ is then resolved (8 cells are needed to resolve a wavelength). As these are less computer intensive, more simulations are available to determine parameters or explore ranges. High-resolution simulations (850 radial by 2048 theta zones, resolving $\ell = 1 - 512$) are used to examine small wavelength modes. They are needed to resolve growth of hydrodynamic instabilities, which can grow faster at higher spatial frequencies.

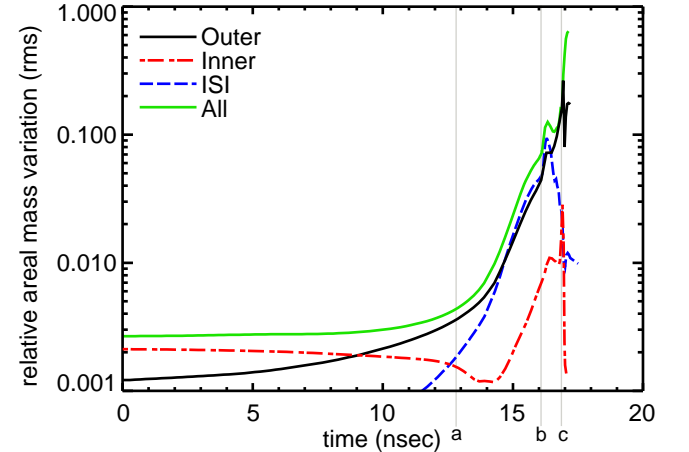


FIG. 8. (Color online) Relative rms perturbation of the areal mass ($\delta \rho R / \rho R$) in the pellet for the scale-2 target with a 300 kJ, 110 TW compression pulse. The solid black line shows the growth of outer surface perturbations (initially $0.48 \mu\text{m}$ rms), the red dash-dotted line is the inner surface perturbation (initially $1 \mu\text{m}$ rms), the blue dash line is for 300 overlapped 1 THz bandwidth ISI beams, all for a 150 kJ ignitor. The green line is for all three perturbation sources simultaneously, and with a 200 kJ ignitor. The vertical gray lines denote the times (a) as the compression shock breaks out of the rear of the fuel shell; (b) as the ignitor shock turns on, and (c) when the pellet stagnates and ignition occurs.

Nominal surface perturbations (both inner and outer) and laser optical smoothing (ISI) generated perturbations are on scale-2 targets in these studies. These nominal levels are as smooth as achievable in the real world. The outer surface perturbations correspond to the surfaces that has been achieved and measured in GDP (glow discharge polymer) plastic

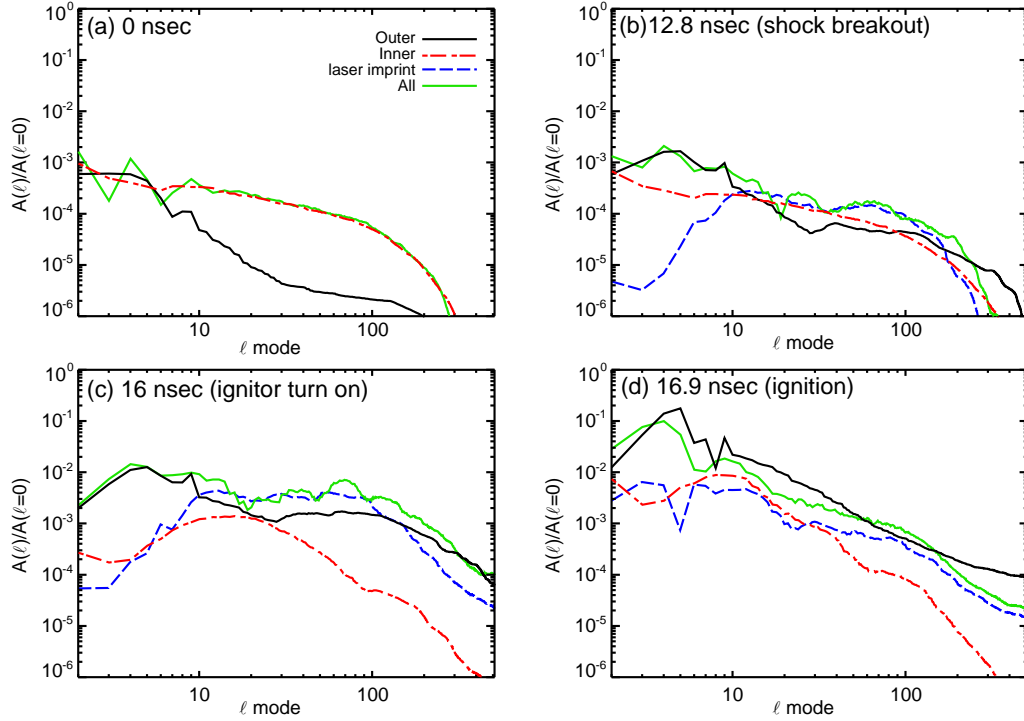


FIG. 9. (Color online) The areal mass perturbation amplitude spectrum, normalized to the average areal mass ($A(\ell=0)$) at four times during the implosion, for the different perturbations sources included here. The different times shown are at (a) $t=0$; (b) 12.8 ns when the shocks break out from the rear of the target; (c) 16 ns, when the ignitor shock turns on; and (d) 16.9 ns, when the pellet ignites. The sources included are perturbation on the outer surface (black), inner surface (red dash-dotted), ISI laser imprint (blue dashed), and all three sources combined at once (green). The modes greater than $\ell = 10$ have been locally averaged in wavenumber from 0.8ℓ to 1.2ℓ to reduce statistical fluctuations that obscure the plot.

shells¹⁸, and have an amplitude given by the formula $A_\ell[nm] = 9600\ell^{-3.39} + 2.4\ell^{-0.78}$ for $\ell > 5$ and $A_\ell[nm] = \min(102 - 4.8(\ell - 1.8)^{2.4}, 100)$ for $\ell < 5$. This is a $0.125 \mu m$ ($\ell = 2 - 2000$) rms perturbation in plastic ($\sim 1 - 1.2 g/cm^3$), or an equivalent areal mass perturbation of $0.48 \mu m$ in the $0.33 g/cm^3$ wicked-foam. The inner DT-ice surface perturbation has the form $A_\ell[nm] = 1000 / (3.0\ell^{0.6} + 2.2 \cdot 10^{-7}\ell^4)$ ¹⁹, and a nominal amplitude of $1 \mu m$ rms. For optical smoothing, we use 1 THz ISI, appropriate for KrF light. (This is similar to 1 THz 2D-SSD smoothing in glass lasers, with the exception that the longer wavelength modes ($\ell \lesssim 20$) are much more smoothed with ISI²⁰). 300 overlapped incoherent beams are chosen to correspond to NRL's Fusion Test Facility proposal²¹, which has 1800 total beams. (The rule of thumb being used is that the average intensity at any given spot on an evenly illuminated pellet is $N/6$ of the intensity from a single beam²², where N is the total number of beams illuminating the pellet).

The simulations predict that target is robust to the separate perturbation sources at nominal amplitude levels, with ignitor power and energy levels comparable to but greater than used to produce the highest 1D gain. For instance, the 1D best gain was found to be 142 for 450 TW, 200 psec full width at half maximum (FWHM) ignitor. 2D high-resolution simulations with nominal outer surface perturbations on this target find an optimum gain of 125 for a 650 TW 200 psec ignitor (the 1D

best gain at 650 TW is 138).

For a fixed laser pulse with a 150 kJ ignitor, the inner DT-ice perturbations can be as large as $3 \mu m$ rms before ignition fails. An outer surface perturbation at twice the nominal level will spoil ignition. However, doubling the ignitor energy to 300 kJ recovers ignition, as the gain drops from 120 to 94 mostly because of this added energy. In general, as the perturbation levels increase ignition eventually fails as the hot spot becomes too perturbed and insufficiently hot to ignite. For perturbation levels that are not too large, increasing the ignitor power restores ignition and gain.

Because of the low initial and in-flight aspect ratio (IFAR), the target is relatively insensitive to the usual high-mode Rayleigh-Taylor growth. Separate simulations including nominal outer or inner perturbations or ISI imprint show that mode growth is not large enough to penetrate the pellet shell, even when amplified by the ignitor shock (Fig. 8). The rms perturbation level of these individual components is below 10% until stagnation and burn occur. All experience a brief jump in their amplitude when the ignitor shock is applied, and generally more rapid growth when the shell decelerates at stagnation. However, the laser imprint evolution is notable because it peaks immediately after the ignitor shock is applied, and then monotonically declines as the shell stagnates.

Differences in the perturbation growth spectra can explain this divergent behavior (Fig. 9). At $t=0$, there is no per-

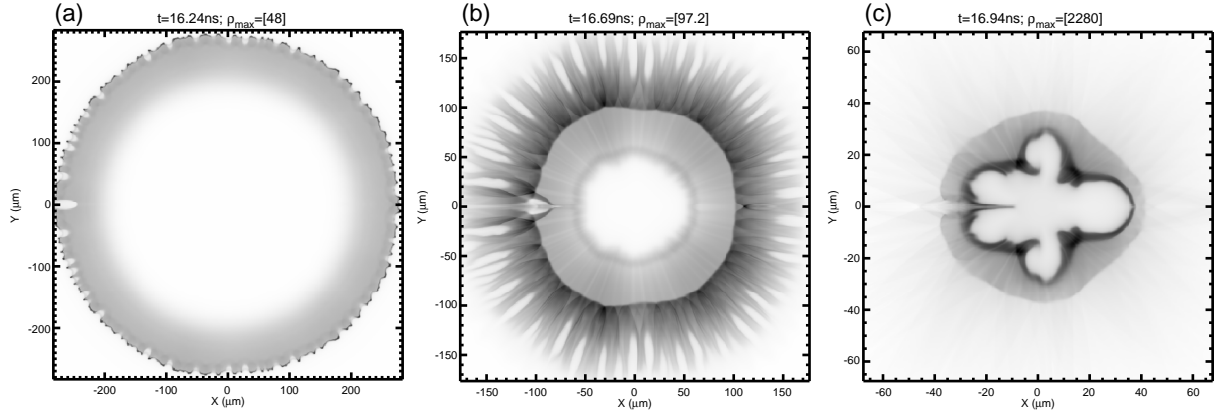


FIG. 10. Images of an imploding pellet at times (a) 100 psec after the ignitor starts; (b) as the ignitor shock is halfway through the shell; (c) at stagnation as the burn begins. The pellet is initially perturbed on the outer and inner surfaces with “NIF-spec” spectra⁴ with nominal amplitudes of $0.48 \mu\text{m}$ and $1.0 \mu\text{m}$ respectively, and was subject to laser imprinting from 300 overlapped mutually incoherent 1 THz ISI beams. The resulting gain is 102.

turbation yet in the laser imprint case; meanwhile the inner and outer perturbation levels are roughly equivalent for $\ell < 10$ while the inner perturbation level is much larger at higher modes. At shock breakout (near the end of Richtmyer-Meshkov growth and before Rayleigh-Taylor (RT) instability begins), both the outer surface and imprint perturbations have grown, while the inner perturbation is unchanged. The imprint has grown larger than the other sources in the range $\ell \sim 10 - 200$.

When the ignitor turns on, the pellet has been driven inward to approximately 40% of its original radius. The growth in this interval is driven mostly by the ablative RT instability in combination with Bell-Plesset effects²³ (Fig. 9c). Imprint is still dominant in the range $\ell \sim 10 - 100$, while the outer perturbation dominates for smaller and larger modes. The inner surface perturbation has grown for $\ell \sim 5 - 70$, but decays for lower modes. This is because growth of the amplitude there is smaller than the growth in ρR due to the spherical convergence.

Finally, at stagnation (Fig. 9d), all growth that affects the ignition and yield has occurred. Compared to the ignitor onset some 900 psec earlier, the spectra are marked by growth in low modes ($\ell \lesssim 10 - 30$) and decay in higher modes. This is consistent with the picture of deceleration RT growth on the inner pellet surface²⁴: higher modes are strongly stabilized by the ablation driven by the forming hot spot. It is also affected by the smaller feedthrough that the higher modes experience between the outer shell (where they were driven by the acceleration stage RT) to the inner edge.

Simulations with the nominal outer, inner, and laser imprint sources combined find that the target will ignite and burn well, but only if the ignitor energy is increased further. For example, the simulation shown in Fig. 10 gives gain ~ 100 for a 1 PW, 200 psec ignitor. Again, the dominant mode at the end of the implosion is the long wavelength $\ell = 5$. The modal spectrum of this simulation is also shown in the Figs. 9. This spectrum roughly forms an envelope over all the other individual perturbations, and confirms that the outer surface perturbation is

the main source of the final low mode structure.

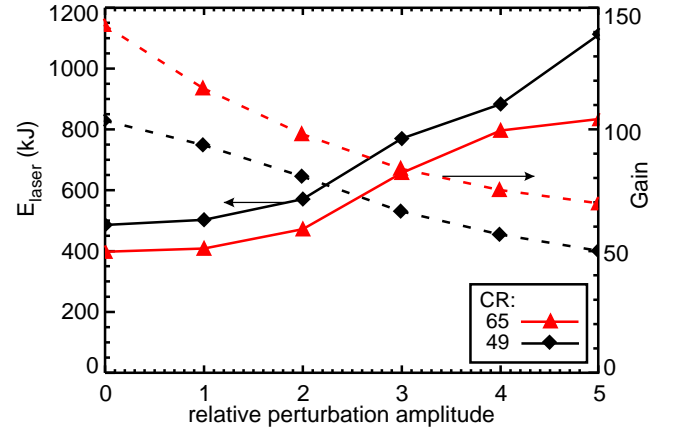


FIG. 11. (Color online) Low-mode ($\ell = 2 - 8$) simulations for target with two different convergence ratios. The perturbation amplitude is measured as a ratio to the nominal perturbation level ($0.48 \mu\text{m}$ rms in the wetted foam). Solid lines are the laser energy used at the optimal gain (left axis), while the dotted lines give the optimal gain (right axis).

A. Convergence Ratio

While the targets here are more stable due to their low IFAR, their convergence ratio (C_r)²⁵ is relatively high (Table I). High C_r targets are more sensitive to low mode target perturbations, which is consistent with the dominant low mode geometry in the stagnated density images (Fig. 10c). These long wavelength modes grow relatively little: classical RT growth is limited to $\lesssim \sqrt{\ell}$ e-foldings, about a factor of 9 for $\ell = 5$. Other growth due to Richtmyer-Meshkov²⁶ or Bell-Plesset²³ is also expected to be small. However, even if the perturbation remains the same, the relative level increases as

$\sim 1/R$. Pressure and mass differences lead to additional secular growth, and scale with C_r (see appendix B). These considerations predict that the initial relative areal mass nonuniformity of a directly-driven pellet should be less than about $0.1/C_r$; for the observed range of $C_r = 50 - 65$ this translates to $\delta\rho R/\rho R < 0.15 - 0.20\%$. The outer surface finish of $0.48\ \mu\text{m}$ rms in the ablator here corresponds to a 0.13% relative areal mass perturbation, and is close to this predicted limit.

We try to mitigate this sensitivity by redesigning the scale-2 target to have a smaller C_r . The approach taken here was to re-time the shocks from the foot pulse and the main pulse to meet slightly inside the fuel shell inner edge. This increases the adiabat there, and pushes more fuel into the low density interior that later forms the hot spot. Advancing the timing of the peak compression power by about $1.2\ \text{nsec}$ decreased C_r from 65 to about 49 for the scale-2 target with 110 TW compression power. It simultaneously decreased the highest 1D gain observed, from ~ 140 to ~ 100 .

Lower resolution ($\ell \sim 2 - 8$) 2D simulations investigate the effect of this redesign on the stability, and the optimum gain is found as a function of perturbation amplitude. Fig. 11 shows the results, which do not reveal any advantage to lowering C_r by this method: the gain is always lower, even at larger perturbations values. The increase in laser energy needed for larger perturbations at both convergence ratios highlights the preferred method of handling perturbations: increase the energy in the ignitor.

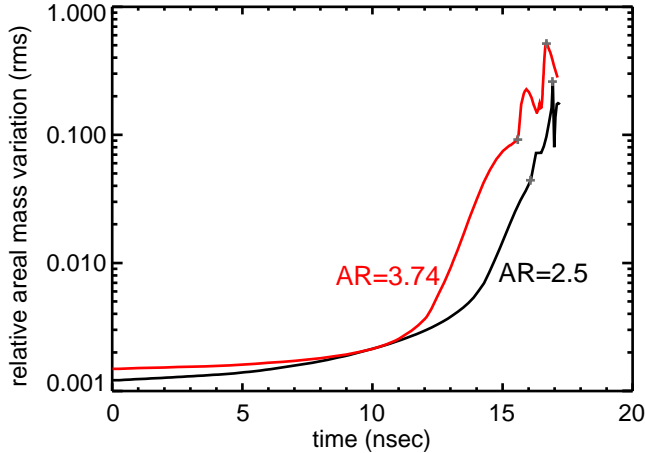


FIG. 12. (Color online) Growth of outer surface modes from high-resolution simulations comparing the original lower aspect ratio target (AR=2.5) with a target that is designed for about 40% lower drive pressure (AR=3.74). The cross marks on the curves denote the time of ignitor turn-on and ignition.

B. Aspect Ratio

In section II C 2, we investigated different targets based on lower drive pressure and intensity. There, we observed that lower intensities lead to higher gains in 1D, but the resulting

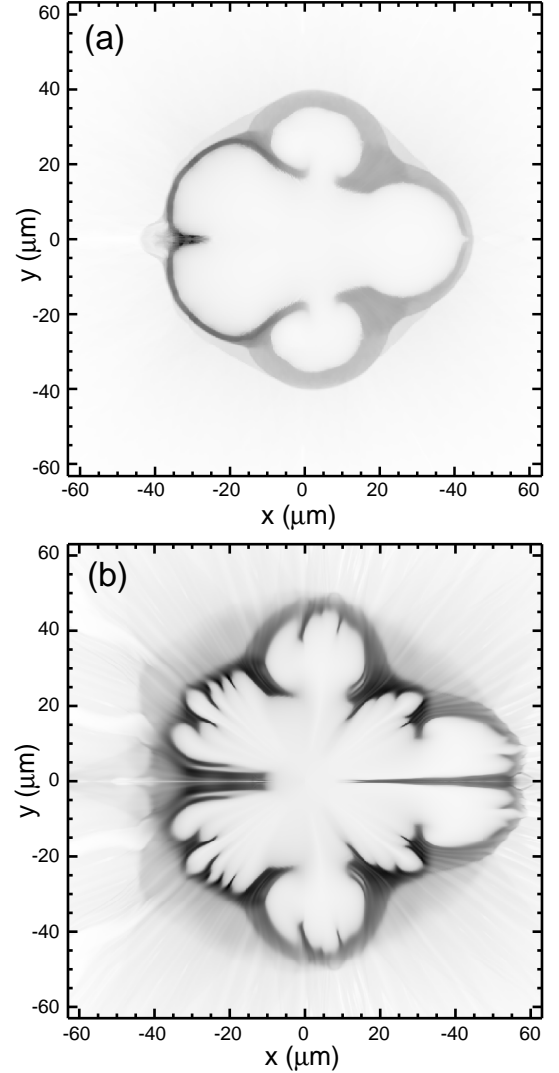


FIG. 13. Images of the imploded density just as the pellet begins to burn (gain is ~ 0.5 at these times) for (a) lower aspect ratio target (AR=2.5) and (b) a higher aspect ratio target (AR=3.7).

higher aspect ratio targets were also projected to be less hydrodynamically stable. Here we quantify this greater instability. High resolution ($\ell = 1 - 512$) is used to resolve the RT growth during the implosion of $\sim 500\text{kJ}$ target with a nominally perturbed outer surface. This target has an initial aspect ratio of 3.74, and is driven with a maximum compression intensity of about $6.6 \times 10^{14}\ \text{W}/\text{cm}^2$ of $0.248\ \mu\text{m}$ light. (For $0.35\ \mu\text{m}$ laser light, it requires $7 \times 10^{14}\ \text{W}/\text{cm}^2$).

Comparing this to the original lower AR target (Fig. 12), the relative rms perturbation growth here is roughly twice as large from the start of the ignitor through to stagnation. Also, the mode structure of the perturbations exhibits an obvious shift to smaller wavelengths (see Fig. 13), indicating that the Rayleigh-Taylor instability is becoming more important. To attain optimum gain, the ignitor energy must be substantially increased to overcome this. For the original AR=2.5 target, the minimum ignitor energy was increased from 70 kJ (1D)

to 130 kJ (2D) to ignite and produce at least gain 100. For the AR=3.74 pellet, the minimum ignitor energy needed to achieve gain > 100 had to be increased from 57 kJ in 1D to 225 kJ in 2D. In addition, the maximum gain observed in 2D for this latter case was about 110, whereas gains of 125 were seen for the lower aspect ratio target with the same perturbations.

IV. CONCLUSIONS

We have investigated low-adiabat shock ignited targets designed to be driven by short wavelength lasers. We use targets imploded with intensities that are close to the limits imposed by LPI, in order to minimize the target aspect ratio and maximize the hydrodynamic stability. We find a robust parameter space for driving these targets as functions of compression power, ignitor power, and timing. The robustness monotonically increases as the energy in the ignitor is increased, both in the 1D and 2D simulations. The efficiency of energy transfer from the component parts of the pulse (the compressor and the ignitor) is also calculated from the simulations. Although the coupling is relatively low for both pulse components, the ignitor couples much more of its energy into the hot spot of the assembled pellet than the compression pulse. Thus, the rudimentary control needed to separately heat the igniting hot-spot independently of producing compression in the cold fuel is present. This control allows one to produce near optimal pellet assemblies, and to ignite pellets at lower drive energies than possible with conventional central ignition. As a result, we find much higher gains for laser energies of less than a megajoule. For optimal gain, the ignitor pulse takes up about 20% of the total laser pulse energy.

The low aspect ratios of these pellets make them more robust to hydrodynamic instabilities. This is possible because the implosion velocities are low (of order 2×10^7 cm/sec), and the pressure applied by the compressing laser is high ($\sim 100 - 300$ Mbar). The latter can only be attained in practice if the compression laser intensity used ($\sim 1.5 - 2 \times 10^{15}$ W/cm²) is not significantly affected by LPI. While this is more likely to be the case for the 0.248 μ m laser wavelength used here, determining the limiting laser intensity is still an area of active research. Current experimental results indicate that this wavelength may allow one to use an intensity that is a factor of ~ 2 higher than the commonly used 0.35 μ m frequency-tripled glass laser wavelength. This work will hopefully spur research needed to determine these intensity limits more accurately.

In these targets, hydrodynamic instabilities produce only mild degradations of the implosion. Instead, low-mode symmetry constraints due to the target's large convergence ratios appear to be the dominant multidimensional effect. In general, these low-mode asymmetries narrow the successful operating space allowed for these targets. Decreasing the convergence ratio through shock timing is not found to be a successful strategy. Instead, a more powerful ignitor can overcome these flaws, although the gain declines somewhat due to the added laser energy.

If the drive pressure must be reduced because of LPI imposed limitations on the compression intensity, then the pellet must have a higher initial aspect ratio. This leads to more susceptibility to hydrodynamic instability. While we have not done an in-depth study of these tradeoffs, we have explored the effect of reducing the intensity by about 40%. We find that the initial aspect ratio then needs to be increased by $\sim 50\%$, and the outer radius by $\sim 20\%$. This higher aspect ratio target allows more mass (for fixed areal density and laser energy) and thus more gain in 1D. However, the target is more Rayleigh-Taylor unstable in 2D, and the higher ignitor energy needed to ignite the more perturbed hot spot leads to a reduced gain overall.

ACKNOWLEDGMENTS

This work was supported by the U.S. Office of Naval Research and the U.S. Department of Energy. We wish to thank Drs. R. Betti and J. Perkins for many useful discussions, and K. Obenshain for his support of the massively parallel computing facilities used for the simulations.

Appendix A: Pellet Assembly Analysis

We follow here the analysis of Meyer-ter-Vehn and others^{15,27,28} and approximate the assembled fuel as a homogeneous hot-spot surrounded by a homogenous mass of compressed fuel. The main difference in the analysis presented here and earlier ones is that we vary the pressure of the compressed fuel instead of the hot spot radius^{15,27} or density²⁸. We explicitly differentiate between the minimum energy required for ignition and the maximum gain, and concentrate on the partitioning of the energy between the hot spot and the cold fuel. Finally, we will examine the differences between the isochoric (fast ignition), isobaric (conventional direct drive) and "mixed" (shock ignition) schemes.

The hot spot energy and mass are determined by the two conditions required for ignition: (1) the ion temperature must be greater than a minimum ignition temperature, $T_{ion} \geq T_{ign} \sim 5$ keV, and (2) the hot spot areal density must be large enough to trap 3.5 MeV alpha particles: $\rho R_h \geq 0.3$ g/cm². Assuming that the pressure and energies in the hot spot can be described by the ideal gas law, and the ion and electron temperatures are equilibrated, the hot spot energy is:

$$E_h [kJ] = 9.54 \times 10^5 \bar{\rho} \bar{R}^3 \bar{T}^3 p_{hGbar}^{-2}. \quad (A1)$$

\bar{T} and $\bar{\rho} \bar{R}$ are the quantities T_{ion} and ρR_h normalized to the nominal values 5 keV and 0.3 g/cm².

The internal energy in the cold compressed fuel is also determined by its pressure. The two constraints that we need, corresponding to the T_{ign} and ρR_h in the hot spot, are the cold fuel mass M_F and the fuel adiabat $\alpha \equiv p/p_{FD}$ where $p_{FD}[Mbar] = 2.2 \bar{\rho}^{5/3}$ is the Fermi-degenerate pressure and $\epsilon_{FD}[MJ/g] = 0.33 \bar{\rho}^{2/3}$ is the Fermi-degenerate energy. Then

$$E_c [kJ] = 3.77 \alpha^{0.6} M_{fmg} p_{Gbar}^{0.4} \quad (A2)$$

where M_{fmg} is the fuel mass in mg. α includes ion pressure, and is the stagnation adiabat, not the in-flight adiabat^{29,30}. Any remaining kinetic energy in the imploding shell is ignored, so in this sense this is an analysis of the “optimum” configuration. Here and in the following, the fuel mass is assumed to be in units of mg , the pressure in $Gbar$, and the energy in kJ .

The total energy of the assembled pellet is the sum of the hot-spot and cold-fuel energies, $E_p = E_h + E_c$. For general non-isobaric configurations, the hot-spot and cold-fuel pressures are linked by the ratio: $p_h = \Phi p$ so the energy of the assembled configuration is only a function of the pressure:

$$E_{tot} [kJ] = 9.54 \times 10^5 \bar{\rho} R^3 \bar{T}^3 \Phi^{-2} p_{Gbar}^{-2} + 3.77 \alpha^{0.6} M_{fmg} p_{Gbar}^{0.4} \quad (A3)$$

In conventional ignition, the assembled hot spot is approximately isobaric, since compression stops and the pellet begins to expand when the pressure roughly equilibrates ($\Phi \sim 1$). In the shock ignition case, the assembled pellet occurs when the pressure in the hot spot is higher than in the cold fuel, so we expect $\Phi > 1$.

1. Isobaric or shock ignition fuel assembly

At low pressures the hot spot energy is very large, and the compression energy is negligible (Fig. 14). As the pressure increases, the hot spot energy rapidly decreases, while the compression energy increases. Conversely, at high pressures the compression energy is dominant and increasing with pressure. This implies an optimum (minimum) assembled pellet energy as a function of pressure, which is found at the point

$$\left(\frac{\partial E}{\partial p} \right)_{M_f, \alpha} = 0, \quad (A4)$$

and occurs where

$$\left. \frac{E_c}{E_h} \right|_{isobaric} = 5. \quad (A5)$$

The pressure and energy of the pellet at this point are:

$$p^{min} [Gbar] = 347 \bar{\rho} R \bar{T}^{5/4} \alpha^{-1/4} \Phi^{-5/6} M_{fmg}^{-5/12} \quad (A6)$$

$$E_{tot}^{min} [kJ] = 48 \bar{\rho} R \bar{T}^{1/2} \alpha^{1/2} \Phi^{-1/3} M_{fmg}^{5/6} \quad (A7)$$

This fully determines all other parameters of the hot spot and cold fuel assembly at the point of minimum energy.

The point of minimum pellet energy would appear to give the optimum assembled pellet. However, we take the optimum point to be at the maximum pellet gain, which is near (but not at) this point. (The gain here is defined as the ratio of the yield to the energy of the assembled configuration). Assuming a burn up fraction given by $f_{burn} = 7/(7 + \rho R_{tot})$, Fig. 14 shows that the point of maximum gain is shifted from minimal assembled energy to a higher energy. The increased yield due to a larger ρR more than compensates for the increased energy used to create the configuration.

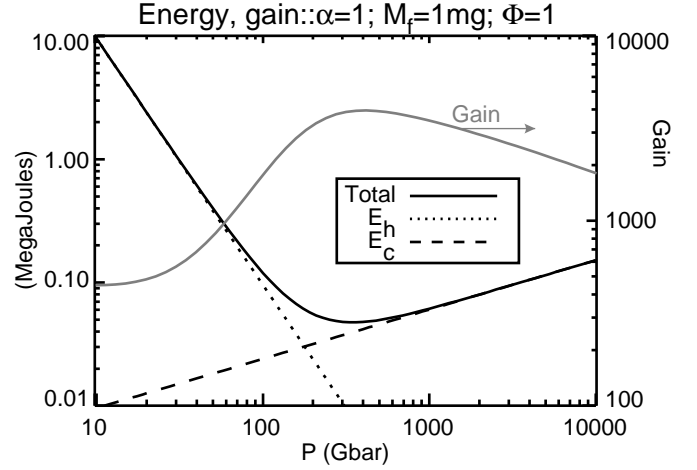


FIG. 14. For the isobaric pellet assembly ($\Phi = 1$), the total and component energies of the pellet assembly as a function of assembly pressure. The fuel assembly gain (gray curve, with axis at right) is also shown. Note that the peak gain occurs at a pressure that is greater than that at the point of minimum total energy.

The parameters at the point of maximum gain can be found using an analysis that mirrors Rosen’s²⁷, but using energy instead of the hot spot radius as the independent parameter. We first make the approximations: (1) $E_{kj} \simeq E_c \gg E_h$; and (2) the burnup fraction can be approximated by the simple power law, $f_{burn} \sim \frac{1}{2}(\rho R/7)^{1/2}$. Then the assembly gain is

$$G = 335.3 \times 10^3 f_{burn} M_{mg} / E_{kJ} \approx 63366 M_{mg} \frac{(\rho R)^{1/2}}{E_{kj}} \quad (A8)$$

With the first assumption we can relate the cold fuel pressure and density and the hot-spot density to the cold fuel energy:

$$\begin{aligned} p [Gbar] &= 0.036 \alpha^{-3/2} M_{mg}^{-5/2} E_c^{5/2} \\ \rho_c &= 5.45 (E_c / \alpha M_{mg})^{3/2} \\ \rho_h &= 0.0095 \frac{\Phi}{\bar{T} \alpha^{3/2} M_{mg}^{5/2}} E_c^{5/2}. \end{aligned}$$

Then it follows that:

$$R_h = r_0 E_c^{-5/2} \quad (A9)$$

$$R_c \simeq r_1 E_c^{-1/2} \quad (R_h^3 \ll R_c^3) \quad (A10)$$

$$\rho R_{tot} \simeq 5.45 (\alpha M_{mg})^{-3/2} E_c \times [r_1 - r_0 E_c^{-2}] + 0.3 \bar{\rho} \bar{R} \quad (A11)$$

$$G \simeq 63366 M_{mg} \left(5.45 (\alpha M_{mg})^{-3/2} E_c^{-1} \times [r_1 - r_0 E_c^{-2}] + 0.3 \bar{\rho} \bar{R} E_c^{-2} \right)^{1/2} \quad (A12)$$

where we have defined the parameters

$$r_1 \equiv 0.035 \alpha^{1/2} M_{mg}^{5/6} \text{ cm} - kJ^{1/2} \quad (A13)$$

and

$$r_0 \equiv 31.7 \bar{\rho} R \bar{T} \alpha^{3/2} M_{mg}^{5/2} \Phi^{-1} \text{ cm} - kJ^{5/2}. \quad (A14)$$

We have also assumed that the cold compressed fuel volume is much larger than the hot-spot in the equations above.

The maximum gain occurs at $\partial G/\partial E = 0$ while holding α , Φ , and M_{mg} constant. The energy at maximum gain is then $E^* = \sqrt{3r_0/r_1}$, or:

$$E_{kJ}^* = 52 \overline{\rho R T}^{1/2} \alpha^{1/2} M_{mg}^{5/6} \Phi^{-1/2} \quad (\text{A15})$$

where we have assumed $\rho R \gg 0.3 \overline{\rho R}$. This gives the maximum gain:

$$G^* = 3150 \overline{\rho R T}^{-1/4} M_{mg}^{1/4} \alpha^{-3/4} \Phi^{1/4} \quad (\text{A16})$$

We can also write the optimum mass as a function of energy by solving Eqn. (A15) for the mass:

$$M_{mg}^* = 0.0087 \overline{\rho R T}^{-3/5} \alpha^{-3/5} \Phi^{3/5} E_{kJ}^{6/5} \quad (\text{A17})$$

Other parameters of the pellet at the peak gain point are found by using the expressions for E_{kJ}^* or M_{mg}^* ; they are listed in tables II and III. We note one curiosity: at the point of maximum gain, the assembly aspect ratio is constant, independent of all other parameters: $R_c/R_H = \frac{r_1}{r_0} E^{*2} = 3$.

2. Isochoric fuel assembly

In the case of isochoric assemblies, $\rho_h = \rho_c$ and the ratio of pressures between the hot spot and cold fuel is a function of the cold fuel pressure $\Phi = \Phi(p)$:

$$\Phi = 153 \overline{T} \alpha^{-3/5} p^{-2/5}.$$

Equivalently, we can write this ratio as a function of the cold energy:

$$\Phi = 575 \overline{T} M_{mg} / E_c.$$

Because of this functional dependence of Φ on E_c , the minimum energy changes from the previous result. The ratio of the energies at the minimum energy point becomes:

$$\left. \frac{E_c}{E_h} \right|_{\text{isochoric}} = 3 \quad (\text{A18})$$

which matches the result found in Eliezer et al.²⁸. The pressure and energy at this point can be calculated by using Eqn. (A3). First, rewrite the hot-spot energy equation (A1) as modified by the relation $\Phi = \Phi(p)$:

$$E_h = 41 \overline{\rho R^3 T} \alpha^{6/5} p^{-6/5}. \quad (\text{A19})$$

Then the cold pressure at the minimum energy is:

$$p^{\min} = 8.8 \overline{\rho R}^{15/8} \overline{T}^{5/8} M_{mg}^{-5/8} \alpha^{3/8}$$

Using Eqn. (A2) and $E_{\text{total}} = \frac{4}{3} E_c$, the minimum energy is

$$E_{\text{total}}^{\text{isochoric-min}} [kJ] = 12 \overline{\rho R}^{3/4} \overline{T}^{1/4} \alpha^{3/4} M_{mg}^{3/4} \quad (\text{A20})$$

Turning our attention now to the parameters needed for optimum gain, we notice that the expression for ρR_{tot} can be

simplified in the isochoric case: $\rho R_{\text{tot}} = \rho_c R_c$. The radius is still given by eqn. (A10), so:

$$\rho R_{\text{tot}} \simeq 5.45 (\alpha M_{mg})^{-3/2} r_1 E_c \quad (\text{A21})$$

$$G \simeq 27770 \alpha^{-1/2} M_{mg}^{2/3} E_c^{1/2} / (E_c + E_h) \quad (\text{A22})$$

In the isochoric assembly, E_h can no longer be neglected compared to E_c in the equation for gain. The gain can be simplified if we express E_h as a function of E_c (using Eqn (A19)):

$$E_h = 2190 \overline{\rho R^3 T} \alpha^3 M_{mg}^3 E_c^{-3}$$

so that

$$G \simeq 27770 \alpha^{-1/2} M_{mg}^{2/3} E_c^{1/2} / (E_c + e_3 E_c^{-3}) \quad (\text{A23})$$

where $e_3 \equiv 2190 \overline{\rho R^3 T} \alpha^3 M_{mg}^3$. Then the maximum gain is found from:

$$\frac{\partial G}{\partial E_c} = 0 = \frac{7}{2} \frac{G}{E_c} - \frac{4 G E_c^3}{E_c^4 + e_3}$$

which has the root:

$$E_c^* = (7e_3)^{1/4}$$

or:

$$E_c^* = 11 \overline{\rho R^3 T}^{1/4} \alpha^{3/4} M_{mg}^{3/4}.$$

Note that at this point, $E_h^* = e_3 / E_c^{*3} = \frac{1}{7} E_c^*$, so that $E_{kJ}^* = \frac{8}{7} E_c^*$ at maximum gain, or:

$$E_{kJ}^* = 12.7 \overline{\rho R^3 T}^{1/4} \alpha^{3/4} M_{mg}^{3/4}. \quad (\text{A24})$$

Invert this to express the optimal mass in terms of the total energy:

$$M_{mg}^* = 0.0337 \overline{\rho R}^{-1} \overline{T}^{-1/3} \alpha^{-1} E_{kJ}^{4/3}. \quad (\text{A25})$$

Other parameters at the point of peak gain can be found in tables II and III.

Appendix B: low mode uniformity limits and convergence ratio

We consider here the prospect of low ℓ mode perturbations distort the imploded core of an ICF target and spoiling gain. We will ignore the Rayleigh-Taylor instability (its growth rate is $\sim \sqrt{\ell}$) and consider only the secular growth of initial perturbations. Beginning with the rocket equation³¹ the implosion velocity is $v = \frac{P}{\dot{m}} \ln[m(t)/m_0]$, where $m(t)$ is the target areal mass, m_0 is the initial target areal mass, P is the driving pressure, and \dot{m} is the target velocity. The implicit assumption is that P and the mass ablation rate, \dot{m} , are constant, so $m(t) = m_0 - \dot{m}t$, or $t = \frac{m_0}{\dot{m}} - \frac{m(t)}{\dot{m}} = (1 - X)/\dot{X}$, where $X \equiv m(t)/m_0$. The distance pushed is then

$$R \sim vt = \frac{P}{\dot{m}_0} \ln X (1 - X) / \dot{X}^2. \quad (\text{B1})$$

TABLE II. Fuel assembly parameters at peak gain, expressed as a function of mass M_{mg} .

parameter	Isobaric / Shock Ignition	Isochoric
E_{kJ}	$52 \bar{\rho} \bar{R} T^{1/2} \alpha^{1/2} M_{mg}^{5/6} \Phi^{-1/2}$	$13 \bar{\rho} \bar{R}^{3/4} \bar{T}^{1/4} \alpha^{3/4} M_{mg}^{3/4}$
E_c/E_h	$27/\Phi$	7
p [Gbar]	$705 \bar{\rho} \bar{R} T^{5/4} \alpha^{-1/4} M_{mg}^{-5/12} \Phi^{-5/4}$	$15 \bar{\rho} \bar{R}^{15/8} \bar{T}^{5/8} \alpha^{3/8} M_{mg}^{-5/8}$
p_h/p	Φ	$52 \bar{\rho} \bar{R}^{-3/4} \bar{T}^{3/4} \alpha^{-3/4} M_{mg}^{1/4}$
ρ_c	$2037 \bar{\rho} \bar{R} T^{3/4} \alpha^{-3/4} M_{mg}^{-1/4} \Phi^{-3/4}$	$202 \bar{\rho} \bar{R}^{9/8} \bar{T}^{3/8} \alpha^{-3/8} M_{mg}^{-3/8}$
ρ_h/ρ_c	$0.09 \bar{\rho} \bar{R}^{1/2} \bar{T}^{-1/2} \alpha^{1/2} M_{mg}^{-1/6} \Phi^{1/2}$	1
$R_h(\mu m)$	$16 \bar{\rho} \bar{R} T^{-1/4} \alpha^{1/4} M_{mg}^{5/12} \Phi^{1/4}$	$15 \bar{\rho} \bar{R}^{-1/8} \bar{T}^{-3/8} \alpha^{3/8} M_{mg}^{3/8}$
$R_c(\mu m)$	$3 R_h$	$106 \bar{\rho} \bar{R}^{-3/8} \bar{T}^{-1/8} \alpha^{1/8} M_{mg}^{11/24}$
Gain	$3150 \bar{\rho} \bar{R} T^{-1/4} \alpha^{-3/4} M_{mg}^{1/4} \Phi^{1/4}$	$7280 \bar{\rho} \bar{R}^{-3/8} \bar{T}^{-1/8} \alpha^{-7/8} M_{mg}^{7/24}$

TABLE III. Fuel assembly parameters at peak gain, in terms of total energy.

parameter	Isobaric / Shock Ignition	Isochoric
M_{mg}	$0.0087 \bar{\rho} \bar{R} T^{-3/5} \alpha^{-3/5} \Phi^{3/5} E_{kJ}^{6/5}$	$0.034 \bar{\rho} \bar{R}^{-1} \bar{T}^{-1/3} \alpha^{-1} E_{kJ}^{4/3}$
E_c/E_h	$27/\Phi$	7
p [Gbar]	$5080 \bar{\rho} \bar{R} T^{3/2} \Phi^{-3/2} E_{kJ}^{-1/2}$	$132 \bar{\rho} \bar{R}^{5/2} \bar{T}^{5/6} \alpha E_{kJ}^{-5/6}$
p_h/p	Φ	$22 \bar{\rho} \bar{R}^{-1} \bar{T}^{2/3} \alpha^{-1} E_{kJ}^{1/3}$
ρ_c	$6660 \bar{\rho} \bar{R} T^{9/10} \alpha^{-3/5} \Phi^{-9/10} E_{kJ}^{-3/10}$	$720 \bar{\rho} \bar{R}^{3/2} \bar{T}^{1/2} E_{kJ}^{-1/2}$
ρ_h/ρ_c	$0.2 \bar{\rho} \bar{R}^{-3/5} \bar{T}^{-2/5} \alpha^{3/5} \Phi^{2/5} E_{kJ}^{-1/5}$	1
$R_h(\mu m)$	$2.3 \bar{\rho} \bar{R} T^{-1/2} \Phi^{1/2} E_{kJ}^{1/2}$	$4.2 \bar{\rho} \bar{R} T^{-1/2} E_{kJ}^{1/2}$
$R_c(\mu m)$	$3 R_h$	$22 \bar{\rho} \bar{R}^{-5/6} \bar{T}^{-5/18} \alpha^{-1/3} E_{kJ}^{11/18}$
Gain	$963 \bar{\rho} \bar{R} T^{-2/5} \alpha^{-9/10} \Phi^{2/5} E_{kJ}^{3/10}$	$2710 \bar{\rho} \bar{R}^{-2/3} \bar{T}^{-2/9} \alpha^{-7/6} E_{kJ}^{7/18}$

Different drivers give different mass ablation rates and mass remaining at the time of stagnation. Typical values for final mass are $X_{final} \approx 0.5 - 0.7$ for direct-drive and $X_{final} \approx 0.2$ for indirect-drive targets³¹.

1. Sensitivity to initial target mass asymmetry

First consider asymmetry due to surface perturbations or initial areal mass perturbations. (Thus, inner-surface or outer-surface, or volume perturbations, are considered to be the same). We wish to find the variance in the throw distance, R , as a function of mass perturbation. (This variance, when compared to the assembled target size, should give us a measure of sensitivity). Using the chain rule and the relations $\partial \dot{X}/\partial m_0 = -\dot{X}/m_0$ and $\partial X/\partial m_0 = (1-X)/m_0$, we find

$$\frac{dR}{dm_0} = \frac{R}{m_0} \frac{1-X}{X \ln X} \quad (B2)$$

or:

$$\frac{dR}{R} = -\frac{X-1}{X \ln X} \frac{dm_0}{m_0} = -f_1(X) \frac{dm_0}{m_0}. \quad (B3)$$

The function $f_1(X)$ relating the core distortion and the initial mass asymmetry is shown in Fig. 15. The initial perturbation dm_0/m_0 must be *smaller* as the ablated mass increases.

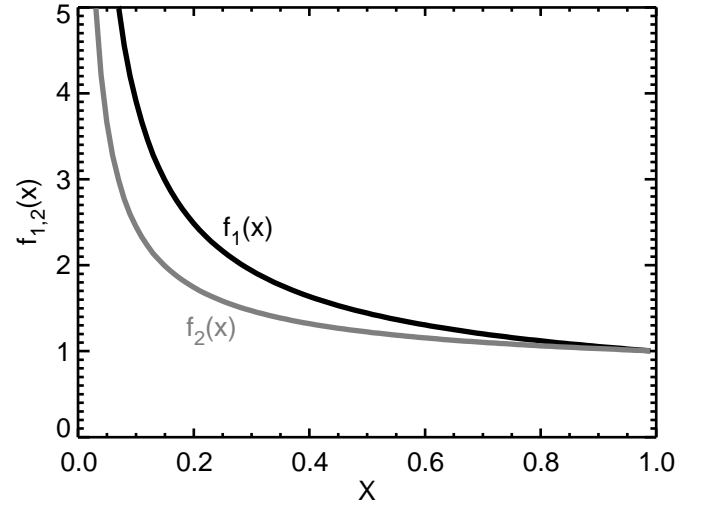


FIG. 15. The function $f_1 = \frac{X-1}{X \ln X}$ describes the sensitivity of the core radius to initial mass perturbations, whereas the function $f_2 = (1+f_1)/2$ (in gray) describes the sensitivity of the final target mass to pressure perturbations.

The allowable initial target mass perturbation is determined by the design constraint that the variation in push distance (dR) should be significantly smaller than the assembled hot

spot (R_h). Defining the pellet convergence ratio as $C_r = R/R_h$, the relevant criteria is:

$$\frac{dR}{R_h} = C_r f_1(X) \frac{dm_0}{m_0} \ll 1 \quad (\text{B4})$$

...for some meaning of “ $\ll 1$ ”. Lindl³² notes that it depends on the ignition margin available, and states that for the NIF ignition capsules it means “ $< 1/4$ ”. This is roughly consistent with the results found here. So we are left with:

$$\frac{dm_0}{m_0} < \frac{1}{4C_r f_1(X)} \quad (\text{B5})$$

For constant density shell targets, $dm_0/dm = dr/\Delta R$ where dr is the surface finish and ΔR is the shell thickness. Typical convergence ratios for ICF targets can range from 25-45, depending upon the particular target, but the shock ignition targets here have larger C_r .

2. Pressure asymmetry limits

A separate issue is the effect of low-mode drive pressure asymmetries. We can repeat the previous analysis but consider the sensitivity to drive pressure, P . We use eqn. B1, and also note that $\dot{X} \sim \sqrt{P}$ ³¹. Then the variance of the distance pushed with respect to the driving pressure is given by:

$$\frac{dR}{R} = \frac{1}{2} \left[1 - \frac{1-X}{X \ln X} \right] \frac{dP}{P} \equiv f_2(X) \frac{dP}{P} \quad (\text{B6})$$

The function $f_2(X)$ is shown in Fig.15. This leads to the following constraint on low-mode pressure variation:

$$\frac{dP}{P} < \frac{1}{4C_r f_2(X)} \quad (\text{B7})$$

The allowed relative pressure variation is somewhat greater than the mass variation, although the effect is only appreciable as $X \Rightarrow 0$.

- ¹V. A. Shcherbakov, Sov. J. Plasma Phys. **9**, 240 (1983).
- ²R. Betti, C. D. Zhou, K. S. Anderson, L. J. Perkins, W. Theobald, and A. A. Solodov, Phys. Rev. Lett. **98**, 155001, (2007).
- ³X. Ribeyre, G. Schurtz, M. Lafon, S. Galera and S. Weber, Plasma Phys. Contr. Fus. **51**, 015013 (2009).
- ⁴A. J. Schmitt, J. W. Bates, S. P. Obenschain, S. T. Zalesak, D. E. Fyfe, and R. Betti, Fusion Sci. Technol. **56**, 377 (2009); J. W. Bates, A. J. Schmitt, D. E. Fyfe, S. P. Obenschain, and S. T. Zalesak, “Simulations of high-gain shock-ignited inertial-confinement-fusion implosions using less than 1 MJ of direct KrF-laser energy” Journal of High Energy Density Physics, in press (2010) doi:10.1016/j.hedp.2009.12.002.
- ⁵B. Yaakobi, C. Stoeckl, W. Seka, J. A. Delettrez, T. C. Sangster, and D. D. Meyerhofer, Phys. Plasmas **12**, 062703 (2005).
- ⁶C. Stoeckl, R. E. Bahr, B. Yaakobi, W. Seka, S. P. Regan, R. S. Craxton, J. A. Delettrez, R. W. Short, J. Myatt, A. V. Maximov, and H. Baldis, Phys. Rev. Lett. **90**, 235002 (2003).
- ⁷W. Seka, D. H. Edgell, J. F. Myatt, A. V. Maximov, R. W. Short, V. N. Goncharov, and H.A. Baldis, Phys. Plasmas **16**, 052701 (2009).
- ⁸J. L. Weaver, J. Oh, L. Phillips, B. Afeyan, J. Seely, D. Kehne, C. Brown, S. Obenschain, V. Serlin, A. J. Schmitt, U. Feldman, G. Holland, R. H. Lehmborg, E. McLean, and C. Manka, “Observations of the Two Plasmon Decay Instability Driven by the Nike KrF Laser” submitted to Physical Review Letters.
- ⁹J. L. Weaver, J. Oh, B. Afeyan, L. Phillips, J. Seely, U. Feldman, C. Brown, M. Karasik, V. Serlin, Y. Aglitskiy, A. N. Mostovych, G. Holland, S. Obenschain, L.-Y. Chan, D. Kehne, R. H. Lehmborg, A. J. Schmitt, D. Colombant, A. Velikovich, Phys. Plasmas **14**, 056316 (2007).
- ¹⁰R. Betti, W. Theobald, C. D. Zhou, K. S. Anderson, P. W. McKenty, S. Skupsky, D. Shvarts, V. N. Goncharov, J. A. Delettrez, P. B. Radha, T. C. Sangster, C. Stoeckl and D. D. Meyerhofer, J. Phys.: Conf. Ser. **112**, 022024 (2008).
- ¹¹L. J. Perkins, R. Betti, K. N. LaFortune, and W. H. Williams, Phys. Rev. Lett. **103**, 045004 (2009).
- ¹²J. H. Gardner, A. J. Schmitt, J. P. Dahlburg, C. J. Pawley, S. E. Bodner, S. P. Obenschain, V. Serlin and Y. Aglitskiy, Phys. Plasmas **5**, 1935 (1998).
- ¹³K. Anderson and R. Betti, Phys. Plasmas **10**, 4448 (2003); R. Betti, K. Anderson, J. Knauer, T. J. B. Collins, R. L. McCrory, P. W. McKenty, and S. Skupsky, Phys. Plasmas **12**, 042703 (2005).
- ¹⁴The first zoom occurs as the pulse attains peak compression power, and the second when the ignitor turns on. The zoom ratios (ratio of the spot size after the zoom to the original laser spot size) are chosen to be the ratio of the critical surface radius (at the zoom time) to the original pellet radius. The zoom ratios here are 0.63 and 0.41.
- ¹⁵J. Meyer-ter-Vehn, Nucl. Fusion **22**, 561 (1982).
- ¹⁶R. H. Lehmborg, J. A. Giuliani, and A. J. Schmitt, Journal Appl. Phys. **106**, 023103 (2009).
- ¹⁷In general, we use $V^2 \equiv I^{0.78} R / \rho \Delta R$, $T \equiv R/V$, $E \equiv IR^2 T$, and $\dot{m} \equiv I^{1/3} T$, where I =intensity, R =Radius, V =Velocity, T =Driver Pulse Width (characteristic time), and $\rho \Delta R$ is the target areal mass. This assumes planar geometry. The scalings in the paper are for E and V constant.
- ¹⁸A. Nikroo, J. Bousquet, R. Cook, B. W. McQuillan, R. Paguio, and M. Takagi, Fus. Sci. Tech. **45**, 165 (2004).
- ¹⁹T. Dittrich, S. W. Haan, M. M. Marinak, S. M. Pollaine, and R. McEachern, Phys. Plasmas **5**, 3708 (1998).
- ²⁰R. H. Lehmborg and J. E. Rothenberg, J. Appl. Phys. **87**, 1012 (2000).
- ²¹S. P. Obenschain, D. G. Colombant, A. J. Schmitt, J. D. Sethian and M. W. McGeoch, Phys. Plasmas **13**, 056320 (2006); S. P. Obenschain, J. D. Sethian and A. J. Schmitt, Fus. Sci. Technol. **56**, 594 (2009).
- ²²A.J. Schmitt, Appl. Phys. Lett. **44**, 399 (1984).
- ²³G. I. Bell, Los Alamos Scientific Laboratory Report No. LA-1321, (1951); M. S. Plesset, J. Appl. Phys. **25**, 96 (1954); P. Amendt, J. D. Colvin, J. D. Ramshaw, H. F. Robey, and O. L. Landen, Phys. Plasmas **10**, 820 (2003); R. Epstein, Phys. Plasmas **11**, 5114 (2004).
- ²⁴V. Lobatchev and R. Betti, Phys. Rev. Lett. **85**, 4522 (2000); R. Betti, M. Umansky, V. Lobatchev, V. N. Goncharov, and R. L. McCrory, Phys. Plasmas **8**, 5257 (2001); S. Atzeni, A. Schiavi, and M. Temporal, Plasma Phys. Contr. Fus. **46**, B111 (2004); J. Sanz and R. Betti, Phys. Plasmas **12**, 042704 (2005).
- ²⁵The convergence ratio is defined as the ratio of the initial outer target radius to the smallest hot spot radius before or at ignition. The hot spot radius is where the interior density is the average of the peak density and the density at $r = 0$. Ignition is defined when all fuel in an areal density of 0.3 gm/cm^2 reaches at least 4 keV ion temperature.
- ²⁶A. L. Velikovich, J. P. Dahlburg, A. J. Schmitt, J. H. Gardner, L. Phillips, F. L. Cochran, Y. K. Chong, G. Dimonte, and N. Metzler, Phys. Plasmas **7**, 1662 (2000); A.L. Velikovich, A. J. Schmitt, J.H. Gardner, and N. Metzler, Phys. Plasmas **8**, 592 (2001).
- ²⁷M. D. Rosen, J. D. Lindl, and A. R. Theissen, LLNL Laser Program Annual Report, No. UCRL-50021-83, pp. 3-5 (1983).
- ²⁸S. Eliezer, M. Murakami, and J. M. Martinez-Val, Laser Particle Beams **25**, 585 (2007).
- ²⁹R. Betti, K. S. Anderson, V. N. Goncharov, R. L. McCrory, D. D. Meyerhofer, S. Skupsky, and R. P. J. Town, Phys. Plasmas **9**, 2277 (2002).
- ³⁰A. Kemp, J. Meyer-ter-Vehn, and S. Atzeni, Phys. Rev. Lett. **86**, 3336 (2001).
- ³¹M. Rosen, Phys. Plasmas **6**, 1690 (1999).
- ³²J. Lindl, P. Amendt, R. L. Berger, S. G. Glendinning, S. H. Glenzer, S. W. Haan, R. L. Kauffman, O. L. Landen, and L. J. Suter, Phys. Plasmas **11**, 339 (2004).